Regular Article

Insects have hairy eyes that reduce particle deposition

G.J. Amador[1], F. Durand[1], W. Mao[1], S. Pusulri[2], H. Takahashi[4], V.-T. Nguyen[4], I. Shimoyama[4], A. Alexeev[1], and D.L. Hu[1,3,a]

[1] Schools of Mechanical Engineering, Georgia Institute of Technology, Atlanta, USA
[2] Biomedical Engineering, Georgia Institute of Technology, Atlanta, USA
[3] Biol. Georgia Institute of Technology, Atlanta, USA
[4] Department of Mechano-Informatics, The University of Tokyo, Tokyo, Japan

Abstract. An insect's eyes may make up to 40% of its body's surface, and are in danger of being coated by foreign particles such as dust and pollen. To protect them, several insect species possess an array of ocular hairs evenly spaced between each photoreceptor unit. Although these hairs have been observed for over 50 years, their purpose remains a mystery. In this study, we elucidate the function of ocular hairs using a combination of experiments, numerical simulation and micro-fabrication. We measure the eyes of 18 species of insects and find that the length of their ocular hairs is equal to their spacing. We conduct wind tunnel experiments using both an insect eye mimic and an at-scale fabricated micro-pillar array of the same dimensions as the insect eye. Our experiments and simulations show that ocular hairs reduce airflow at the eye surface by up to 90%. We conclude that ocular hairs act similarly to mammalian eyelashes: as insects fly, ocular hairs deflect incoming air and create a zone of stagnant air. Airflow and particle deposition are reduced dramatically, while light is only minimally occluded. Micro-scale ocular hairs may find application in the deployment of sensors outdoors, for which accumulation of airborne dust and pollen has no current solution.

1 Introduction

Flying insects experience the world at high speed, relying on vision to make split-second decisions about predator or obstacle avoidance [1]. The visual response to a fruit fly encountering an obstacle is 50 ms [2], while the visual startle response of a long-legged fly is less than 5 ms [3]. Vision is so important to these insects, that many have compound eyes composed of hundreds to thousands of lenses and nearly 360-degree fields of view. Several insect species have arrays of hairs on their eyes. The fact that they are there is familiar [4], but their function is not well understood.
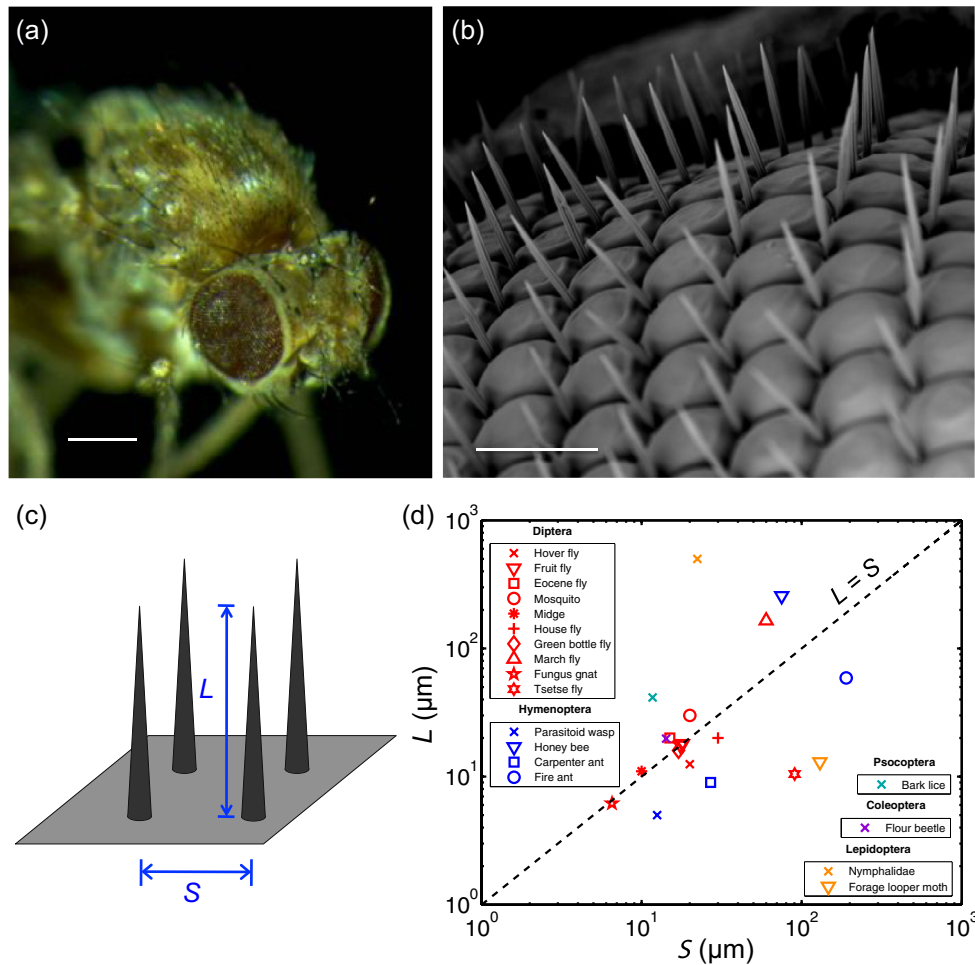
[a] e-mail: hu@me.gatech.edu

Fig. 1. Insect ocular hairs. (a–b) The eye of a fruit fly, *Drosophila melanogaster*. Scale bars represent: (a) 250 μm and (b) 20 μm. (c) Schematic showing geometrical parameters measured. (d) Relationship between hair length L and spacing S for 18 species of insects spanning 5 orders. Dashed line indicates $L = S$. The results are outlined in Table 1.

In this study, we use a combination of experiments, simulation, and micro-fabrication to elucidate a function of the insect ocular hairs.

Most arthropods, like the fruit fly in Fig. 1a, possess compound eyes. Unlike the simple eyes found in vertebrates [5], these are composed of an array of hexagonal photoreceptor units, called ommatidia, and typically look like Fig. 1b. Each ommatidium consists of an individual lens that captures incoming light and transfers the signal to the brain through nerves [6]. In certain insects, like fruit flies and honey bees, hairs have been observed to be present between ommatidia, as shown in Fig. 1b. Although the purpose of these hairs is unknown, previous work has shown that they may play a role in sensing air currents [7,8]. A previous study found that honey bees fly 11% slower when their ocular hairs are shaved, suggesting their potential role in sensing air flow during flight [7,8]. In crickets, these hairs serve as mechanosensors that detect particle accumulation on the eye and trigger head

Table 1. Tabulated hair data for insects and other arthropods, including ocular hair center-to-center spacing S, length L, and thickness h. * Indicates the 6 species of arthropods that are not part of the class *Insecta*. N/A indicates samples where the species name and/or family name were not provided by the source.

Order	Family	Species	Common Name	Hairs present?	S (µm)	L (µm)	h (µm)	Source
Siphonaptera	N/A	N/A	Flea	No				28
Mecoptera	Boreidae	*Caurinus tlagu*	Snow scorpion fly	No				28
Mecoptera	N/A	N/A	Scorpion fly	No				28
Mecoptera	N/A	N/A	Scorpion fly	No				28
Diptera	Syrphidae	*Chrysotoxum intermedium*	Hoverfly	Yes	20.0	12.5	1.3	29
Diptera	Drosophilidae	*Drosophila melanogaster*	Fruit fly	Yes	17.5	17.5	1.5	Here
Diptera	Dolichopodidae	*Neurotexia Primula*	Eocene fly	Yes	15.0	20.0	1.6	30
Diptera	Muscidae	*Musca domestica*	House fly	Yes	30.0	20.0	1.0	31
Diptera	Drosophilidae	*Drosophila virilis*	Fruit fly	Yes	18.0	18.0	1.2	Here
Diptera	Calliphoridae	*Lucilia sericata*	Green bottle fly	Yes	17.0	16.0	1.0	Here
Diptera	Bibionidae	*Bibio johannis*	March fly	Yes	60.0	165.0	2.7	32
Diptera	Glossinidae	*Glossina palpalis*	Tsetse fly	Yes	90.5	10.5	1.8	33
Diptera	Mycetophilidae	*Novakia Miloi*	Fungus gnat	Yes	6.5	6.2	1.4	34
Diptera	Hippoboscidae	N/A	Louse fly	No				28
Diptera	Culicidae	N/A	Mosquito	Yes	20.0	30.0	1.1	35
Diptera	Nematocera	N/A	Midge	Yes	10.0	11.0	1.3	36
Lepidoptera	Nymphalidae	*Aglais io*	Nymphalidae	Yes	22.5	500.0	3.8	37
Lepidoptera	Erebidae	*Caenurgina erechtea*	Forage looper moth	Yes	130.0	13.0	1.0	Here
Coleoptera	Silphidae	*Oxelytrum gistel*		No				38
Coleoptera	Curculionidae	*Sitophilus zeamais*	Maize weevil	No				28
Coleoptera	Scarabaeidae	*Cotinis mutabilis*	Figeater beetle	No				28
Coleoptera	Tenebrionidae	*Tribolium*	Flour beetle	Yes	14.2	19.8	2.4	33
Coleoptera	Histeridae	N/A	Clown beetle	No				28
Coleoptera	Carabidae	N/A	Bombardier beetle	No				28
Coleoptera	Scarabaeidae	N/A	Scarab beetle	No				28
Coleoptera	Coccinellidae	N/A	Lady bug	No				28
Raphidioptera	N/A	N/A	Snakeflies	No				28
Hymenoptera	Trichogrammatidae	*Trichogramma evanescens*	Parasitoid wasp	Yes	12.5	5.0		39
Hymenoptera	Apidae	*Apis melifera*	Honey bee	Yes	75.0	257.0	7.0	Here
Hymenoptera	Formicidae	*Solenopsis invicta*	Fire ant	Yes	189.8	58.9	10.1	40
Phthiraptera	Pediculidae	*Pediculus humanus capitis*	Head louse	No				33
Psocoptera	N/A	N/A	Bark lice	Yes	11.7	41.5	1.4	28
Hemiptera	Cimicidae	*Cimex lectularius*	Bed bug	No				42
Hemiptera	Gerridae	N/A	Water strider	No				43
Hemiptera	Coreidae	N/A	Leaf-footed bug	No				44
Hemiptera	Miridae	N/A	Leaf bug	No				45
Thysanoptera	N/A	N/A	Thrip	No				28
Blattodea	Rhinotermitidae	*Coptotermes elisae*	Termite	No				46
Blattodea	N/A	N/A	Cockroach	No				28
Zoraptera	Zorotypidae	N/A	Angel insect	No				28
Plecoptera	Nemouridae	N/A	Stonefly	No				28
Plecoptera	Peltoperlidae	N/A	Roach like stonefly	No				28
Orthoptera	Rhaphidophoridae	N/A	Camel cricket	No				28
Orthoptera	Gryllidae	*Acheta domesticus*	House cricket	No				28
Phasmatodea	N/A	N/A	Walking stick	No				28
Odanta	Coenagrionidae	N/A	Damslefly	No				28
Odonata	Gomphidae	N/A	Clubtail dragonfly	No				28
Collemobola*	N/A	N/A	Spring tail	No				28
Protura*	N/A	N/A	Proturans	No				28
Diplura*	N/A	N/A	N/A	No				28
Isopoda*	Armadillidiidae	N/A	Pill bug	No				47
Araneae*	Palpimanidae	*Levymanus gershomi*	Spider	No				48
Araneae*	Salticidae	N/A	Jumping spider	No				47

cleaning motions [9]. The short ocular hairs on the eyes of fruit flies develop similarly to sensory hairs, or cilia, and so possess sensory neurons with a branched extension of a nerve cell [10]. In the current study, we focus not on the the ocular hair's sensing ability, but on the effect they have on the incoming flow.

Hair is the ultimate multifunctional structure in both invertebrates and vertebrates, serving a number of important roles in sensing [11–13], insulation [14], protection [15,16], and filtration [17,18]. The hairs on the antennae of moths divert incoming

airflow and stretch its streamlines. By stretching the flow profile, these hairs improve the spatial resolution of the antennae's chemoreception [19,20]. In a previous study, researchers discovered that the bristled wings of thrips also resist airflow and generate sufficient drag-based lift for successful flapping flight [21]. We previously showed that mammalian eyelashes reduce evaporation and accumulation of airborne particulates [22]. In this study, we hypothesize insect ocular hairs serve a similar purpose to mammalian eyelashes by preventing airborne particle accumulation and possibly water loss.

Water management in arthropods is critical for homeostasis, especially because of their large surface area to volume ratios. Greater surface area means the animal is more exposed to the environment and experiences higher rates of exchange, e.g., water loss in dry conditions and moisture absorption in wet conditions. Previous workers have found that, for insects, most of their water is lost through the cuticle [23]. Respiration also accounts for some water loss, but only 5–20% [23]. Since compound eyes contribute a substantial amount to the overall surface area of arthropods, water loss through them may be non-trivial.

In this study, we investigate the function of the ocular hairs of insects. We use experiments and numerical simulations to shed light on the aerodynamics of flow around arrays of hairs similar to those on insects. In Sect. 2, we present our methodology. In Sect. 3.1, we present our measurements of insect ocular hairs. In Sect. 3.2, we present the results of our wind tunnel tests measuring evaporation of insect eye mimics. In Sect. 3.3, we present results of our numerical simulations. In Sect. 3.4, we present our micro-fabrication of ocular hairs of the insect, which we test using wind tunnel experiments. In Sect. 4, we present a discussion of our results and avenues for future work, and provide concluding remarks in Sect. 5.

2 Materials and methods

2.1 Anatomical measurements

We approximate the percentage of surface area taken up by the compound eyes of insects. We use values published in the literature [24,25], as well as unpublished pictures found online showing dorsal views [26–30]. From the pictures, we measure the length and width of the body and the radius of the eyes. Using these measurements, we approximate the body as cylindrical and compound eyes as hemispherical to calculate surface area. When insects fly, they do so headfirst, and so may expose their eyes to great amounts of airflow. To determine the amount of frontal area taken up by the compound eyes, we use unpublished pictures of frontal views [31–35].

Using digital scanning electron microscope (SEM) images from our lab, literature [4,36–43], and unpublished images from the internet [44–55], we observe the eyes of 48 species of insects and 6 species of arthropods that are not part of the class *Insecta*. For the species observed to possess ocular hairs we use SEM images, like the one shown in Fig. 1b, to measure the geometry of the hair arrays, including the hair length L, thickness h, and center-to-center spacing S. The length L and spacing S are shown schematically in Fig. 1c.

2.2 Hairy compound eye mimic

To understand how hairs affect the airflow to the eye of an insect, a replica is constructed in order to perform controlled experiments. To simplify the geometry, the curvature of the eye is neglected and a flat eye surface is used for the mimic.
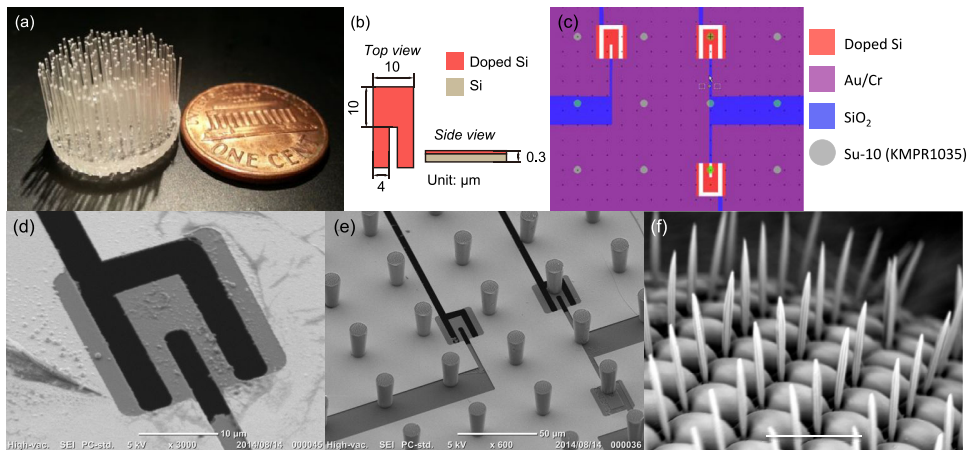
Fig. 2. Mimics of insect ocular hair. (a) Insect ocular hair mimic used in evaporation experiments. (b) Schematic of an individual piezo-resistive cantilever differential pressure sensor. (c) Schematic of one of the masks used to pattern and etch the SOI wafer and thin photoresist layer (KMPR1035). (d) An airflow sensor patterned out of a SOI wafer. (e) SOI wafer with airflow sensors and micro-pillar array. (f) The eye of a fruit fly, for comparison. Scale bars represent: (c) 10 μm, (d) 50 μm, and (e) 20 μm.

For the insect species we observe, the radius of curvature of the eye is roughly one to two orders of magnitude larger than the hair length and spacing, so the eye can be approximated as locally flat. A Phenom G2 Pro SEM is used to obtain images of insect eyes, such as those in Fig. 1b. The images are analyzed using Tracker, an open-source image analysis software by Douglas Brown, to determine the length L and the center-to-center spacing S of the hairs, as shown schematically in Fig. 1c.

In order to construct our insect eye mimic, a Jamieson MT-530 Laser Printer is used to cut out the "eye" surface from an acrylic sheet. A hexagonal array of holes is cut into the eye surface. The holes are used to insert 180 μm-thick glass fibers from fiber optic cables, which represent the hairs. In total, there are 282 protruding fibers, as shown in Fig. 2a. The mimic is then placed inside a cylindrical dish made of plastic (polyoxymethylene, commonly Delrin). Five dishes are used, each with a different depth so that 5 different protruding hair lengths could be easily tested experimentally. The five lengths are approximately $L/S = 1, 2, 3, 4$ and 5.

2.3 Wind tunnel experiments for measuring evaporation

To accurately represent the fluid flow around the insects' eye surfaces, it is important to maintain dynamic similitude. In order to ensure that our experiments accurately represent the flow conditions experienced by flying insects we match the Reynolds number. The Reynolds number Re is the ratio of inertial and viscous forces of the airflow defined by $Re = US/\nu$, where ν is the kinematic viscosity of air, S the spacing of the hairs, and U is the velocity of the air or the flying speed of the insect. From previous literature, the average flight speed of a fruit fly is found to be 2 m s^{-1} [56]. This value is for tethered flight, which gives us a lower bound for a fruit fly's flight speed. Moths and butterflies have been previously observed to travel at speeds of over 13 m s^{-1} [57]. With the reported average tethered speed of the fruit fly and assuming a butterfly or moth could reach a maximum speed of 15 m s^{-1}, the Reynolds numbers based on hair spacing S are calculated to be $Re \approx 9$ and $Re \approx 150$, respectively,

for air at ambient conditions. These Reynolds numbers dictate the minimum and maximum airflow speeds for the experiments.

The airflow to the eye is provided by a small wind tunnel, where parts include: a DC-powered fan, diffuser, honeycombed laminarizer, settling chamber, nozzle, and air-guiding duct. The wind tunnel is the same as the one used in Amador et al. [22]. The eye model is placed in the testing area atop a 10^{-5} g precision scale (Mettler Toledo NewClassic MF, Model MS205DU), with the water-filled dish and protruding hairs facing upwards toward the fan. The plastic dish with the insect ocular mimic is filled with water using a micropipette until the water surface reaches the rim. The water surface represents the eye surface. Each dish and mimic is filled with the same volume of water for each trial. To minimize the water meniscus at each protruding fiber, the fibers were treated with a commercially available hydrophobic spray (Cytonix LLC, WX2100). An optical microscope (Olympus SZX16) was used to verify the minimization of the meniscus.

To simulate the airflow experienced by the fruit fly and moth during flight, the wind speed U is set to 0.11 m/s and 1.1 m/s, respectively. The scale is connected to a computer and a mass reading is taken every 10 seconds for 10 minutes, resulting in 60 total readings per trial. Three trials are conducted for each hair length, including one without hair. The average evaporation rate is found using a least-squares linear regression. Trials are run without any airflow to find the control value for water evaporation, 19.5 μg/s. This value is subtracted from our measured evaporation rates to ensure the rates reported represent only evaporation from the perpendicularly incident flow. The trials were run indoors over a series of weeks in the summer of 2013 in a room of temperature $T = 21.5 \pm 0.5°$C and relative humidity at $RH = 46 \pm 2\%$. The small variance in temperature and humidity allowed for accurate measurements of evaporation rate.

2.4 Numerical methods

We employ a lattice Boltzmann model (LBM) [58–61] to examine the interactions between arrays of hair, the ocular surface, and a viscous flow. The LBM is a mesoscale computational model for simulating hydrodynamic flows governed by the Navier-Stokes equations. The method is based on the time integration of a discretized Boltzmann equation $f_i(\mathbf{r} + \mathbf{c}_i \Delta t, t + \Delta t) = f_i(\mathbf{r}, t) + \Omega[f(\mathbf{r}, t)]$ for a particle's distribution function f. Here, $\mathbf{c}_i$ is the fluid particle's velocity in the direction i at a lattice node $\mathbf{r}$ at time t, Δt is the time step, and Ω is the collision operator accounting for the change in f due to instantaneous collisions at the lattice nodes. The moments of the distribution function are used to calculate fluid density $\rho_a = \sum_i f_i$, the momentum density $j = \sum_i \mathbf{c}_i f_i$, and the stresses $\Pi = \sum_i \mathbf{c}_i \mathbf{c}_i f_i$. We use a three-dimensional 19 velocity model (3D19Q) defined on a simple cubic lattice and a multiple-relaxation-time collision operator [60].

The simulations are conducted in a rectangular computational box large enough that its size does not affect the flow around the eye. The eye is modeled as a circular flat surface with the diameter $12S$ located at the center of a circular face with the diameter $24S$. Each hair is modeled as a sequence of static beads that are uniformly distributed along its length L. Here, we neglect the effect of hair flexibility on the emerging fluid flow.

Frictional force in the form of the Stokes drag $\mathbf{F}_f = -\xi \mathbf{u}_f$ is used to account the effect of hair on the flowing air [62,63]. Here, $\mathbf{u}_f$ is the fluid velocity and $\xi = 6\pi\mu\sigma$ is the drag coefficient with σ being the effective hydrodynamic radius of the seta and μ the dynamic viscosity of air. The force is distributed to LBM nodes surrounding the eyelash using a delta function [64]. Interpolated bounce-back rule is used to impose

the no-slip and no-penetration boundary conditions at the ocular surface [65]. We have previously extensively used LBM to study flows near solid surfaces covered with hair-like filaments [22,66–69].

2.5 Fabrication of airflow sensors within pillar arrays

In this section we present the fabrication techniques used to create micron-scaled pillar arrays with airflow sensors. The pillar arrays are fabricated on top of a SOI (silicon on insulator) wafer with piezo-resistive cantilevers that bend in response to the dynamic pressure of flowing air. A schematic of the cantilever is shown in Fig. 2b. The differential pressure sensors have been used previously by the authors to measure the differential pressure generated by airflows [70,71] and drag generated by an array of bristles [21]. The cantilevers measure the pressure produced by air flowing in between the pillar arrays, so we may use them to measure flow penetration. Details on the fabrication techniques used are outlined in Gel & Shimoyama [72] and Thanh-Vinh et al. [73], but for completeness we will present a brief summary.

The fabrication process begins with a SOI wafer consisting of three layers, a 0.3-μm thick silicon layer on top, then a 0.4-μm thick silicon dioxide layer below, and finally a 300-μm thick silicon layer at the bottom. The top silicon layer of the SOI wafer is doped to change its electrical properties using ion implantation with a dose of $10^{15}\,\text{cm}^{-2}$ of arsenic at 10 keV for 585 seconds and 40 keV for 303 seconds. Thin layers of gold and chromium are deposited through evaporation in a vacuum, with thicknesses of 30 nm and 3 nm, respectively. First, the gold and chromium layers are patterned using photolithography and wet-etching. The top silicon layer is then etched using Inductive Coupled Plasma-RIE (ICP-RIE) using gold and chromium patterns as masks. The etching process reveals the area where the microcantilever will reside, following the mask schematic in Fig. 2c. After that, the piezoresistors at the root of the cantilevers are revealed by patterning and etching the gold and chromium layers. The micropillar array is fabricated by spin coating and patterning a KMPR1035 photoresist (MicroChem Corp, MA, USA) layer with a thickness of 35 μm on top of the wafer. Finally, through holes underneath the cantilever are formed by etching the bottom silicon layer using ICP-RIE and then the silicon dioxide layer are etched by vapor hydrofluoric acid to release the cantilever as shown in Fig. 2b,c. The microcantilever is only made up of the thin layer of doped silicon with a thin gap surrounding it to allow air to flow through and bend the cantilever. SEM images of the final product are shown in Fig. 2d,e. We use three sensors on each wafer, one between the pillars, the other underneath a pillar, and a third without the bottom etched out to measure the change in electrical resistance of the wafer due to the change in temperature.

Qualitatively, the micropillar arrays closely resemble those found interspersed throughout the eyes of flying insects, like the fruit fly shown in Fig. 2f. The pillars are also within the range of geometries of insect ocular hairs. Their length L of 35 μm and thickness h of 5 μm are similar to those observed on insects.

2.6 Wind tunnel experiments with micropillars

We use a small wind tunnel to expose our micro-pillar arrays to airflow. The wind tunnel is fabricated using a 3D printer and is shown in Fig. 3a. The small fan on the left is powered by a DC power supply and pulls air through the wind tunnel. An array of tightly packed straws at the inlet of the wind tunnel (on the right) laminarizes the flow and the nozzle makes it uniform. The velocity U of the flow supplied by the
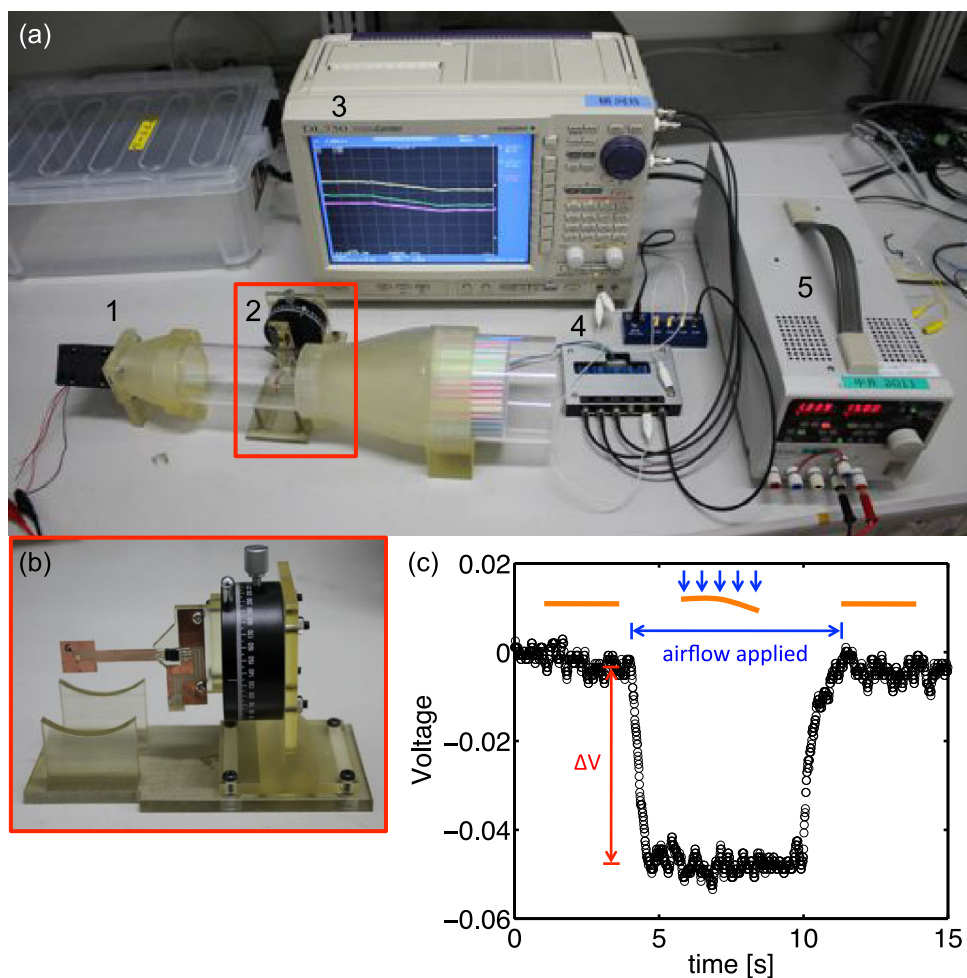
Fig. 3. Wind tunnel experiments with micro-pillars. (a) Experimental setup with *1* small 3D-printed wind tunnel, *2* sensor mount, *3* oscilloscope, *4* signal amplifier with power supply, and *5* DC power supply to power the wind tunnel's fan. (b) Mount holding a wafer with the airflow sensors and micro-pillar array. The mount can rotate about its axis to tilt the wafer and is marked with degree measurements to accurately control the tilt. (c) Relationship between voltage and time when a sensor is exposed to airflow. Top inset shows how the microcantilever sensor bends in response to airflow. The bending causes a change in the electrical resistance and reduces the voltage potential across the sensor.

small fan ensures dynamic similitude with the eye of a fruit fly during flight, or $Re = US/\nu = 10$. The sensor is held inside of the test section using the mount shown in Fig. 3b. This mount allows us to tilt the sensor at an angle with respect to the incoming flow direction. When the microcantilevers are exposed to airflow they bend, as shown in the inset of Fig. 3c. Because they are piezo-resistive, the electrical resistance of the microcantilevers changes as they bend. Using a Wheatstone bridge and amplifier circuit, we apply a potential of 0.5 volt across the cantilever and measure the change in voltage ΔV after being exposed to airflow using an oscilloscope [73]. A typical plot showing the change in voltage ΔV after exposure to airflow is shown

in Fig. 3c. Through calibration experiments using a differential pressure calibrator (KAL100, Halstrup-Walcher GmbH) we find how the voltage difference ΔV varies with the pressure difference ΔP applied. Just like in previous experiments [70,71], we find that there is a linear relationship between them, or $\Delta P \propto \Delta V$. Through the calibration experiments we determine the proportionality constant for each sensor.

3 Results

3.1 Anatomical measurements

Since the majority of water is lost through the cuticle [23], we determine the percentage of total surface area taken up by the compound eyes of arthropods. We find the surface area of the compound eyes makes up 3.3–38% of total surface area, from a midge to a housefly. Therefore, the eyes may contribute to a substantial amount of water loss. This may especially be the case for flying insects that fly headfirst and expose their eyes to impinging airflows. The frontal area, or the area exposed to incoming air during flight, of a flying insect may be 9.1–54% covered by the compound eyes. Thus, a lot of the air striking the insect during flight impacts the eyes directly.

Using our own SEM images, as well as those found in the literature and from unpublished sources, we measure the length L and spacing S of the ocular hairs of arthropods. Of the 54 species observed, only 18 possess ocular hairs, as outlined in Table 1. These species span the 5 orders of insects known to have ocular hairs [74]. In Fig. 1d, we see that the majority of the species observed have a length L that is equal to spacing S. Of the 18 species measured, 10 of them have $0.5 \leq L/S \leq 1.5$. Only 4 out of the 18 species have a length L that is less than half of the spacing S, or $L/S < 0.5$. In the following sections, we present experimental and numerical results that determine how the length of the interspersed ocular hairs affects airflow around the eye.

3.2 Wind tunnel evaporation experiments

Wind tunnel experiments are conducted to determine how the presence of compound eye hairs affects airflow at the eye surface. In these experiments, we measure how the evaporation rate $\dot{m}$ of a small dish of water is affected by an array of hairs similar to those found on fruit flies and moths. A schematic representing our experiments is shown in Fig. 4a. The fluid mechanics between insect hairs is dictated by a local Reynolds number Re based on the spacing S between the hairs and the flight speed U of the insects, found in previous literature [56,57,75–78]. The range of Reynolds numbers Re of the flows encountered by the insects comprising the data in Fig. 1d is $Re = 0.31$–150, from a midge to a moth. For our experiments, we use $Re = 9$ and 150 to represent the dynamic range of values experienced by flying insects, from low to moderate inertial effects.

The results in Fig. 4b show how the the normalized hair length L/S affects the normalized evaporation rate $\bar{\bar{m}}$. We normalize evaporation rate $\dot{m}$ with respect to the values for an eye without hairs $L/S = 0$. The blue and red crosses represent experiments for Reynolds numbers Re of 9 and 150, respectively. They span the dynamic regime of low to moderate Reynolds numbers represented by the insects studied. These results show that airflow at the ocular surface is greatly affected by the presence of hairs.
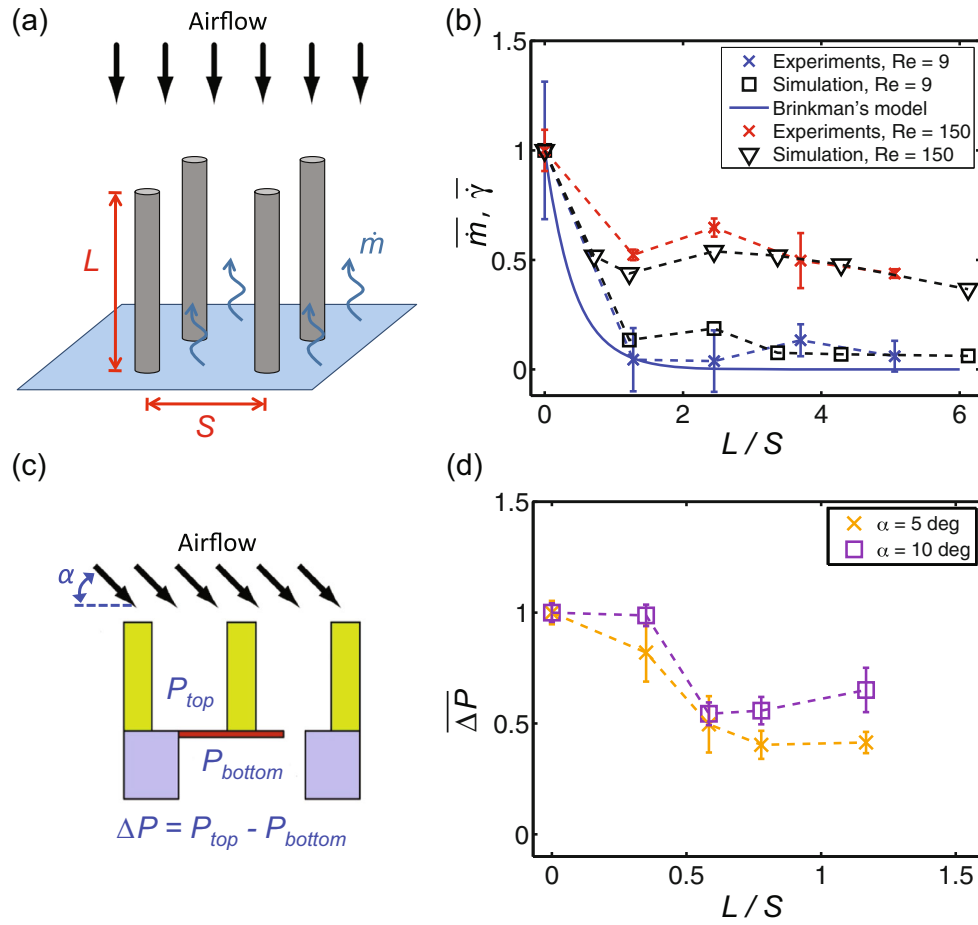
Fig. 4. Experimental and numerical results. (a) Schematic of insect eye hair mimic exposed to airflow perpendicular to the eye's surface. (b) Relationship between normalized evaporation rate $\overline{\overline{m}}$ and dimensionless hair length L/S for experiments (blue and red). Error bars represent the standard error. Relationship between normalized shear rate at eye surface $\overline{\overline{\dot{\gamma}}}$ and dimensionless hair length L/S for simulation (black). The best-fit exponential curve following Brinkman's model is represented by the solid blue line. (c) Schematic of the insect-inspired micro-pillar array exposed to airflow at an angle α. (d) Relationship between normalized differential pressure $\overline{\Delta P}$ and normalized pillar length L/S for different airflow directions α.

3.3 Numerical simulation

We use numerical simulation to verify our experimental results. For convenience, we choose shear rate $\dot{\gamma}$, averaged across the eye surface, as the single metric to characterize the flow. This value is indicative of ocular hair performance because lower shear rate is associated both with lower particle deposition [79] and reduced evaporation [80]. Figure 4b shows how the normalized shear rate $\overline{\overline{\dot{\gamma}}}$ varies with normalized hair length L/S. We normalize shear rate $\dot{\gamma}$ with respect to the values for an eye without hairs $L/S = 0$. The computational results, shown in black in Fig. 4b, match very closely to the experimental data in blue and red, with each simulation lying within the standard error of the experiments. Both experiments and simulation show a drastic decrease in airflow at the ocular surface with the presence of hairs.
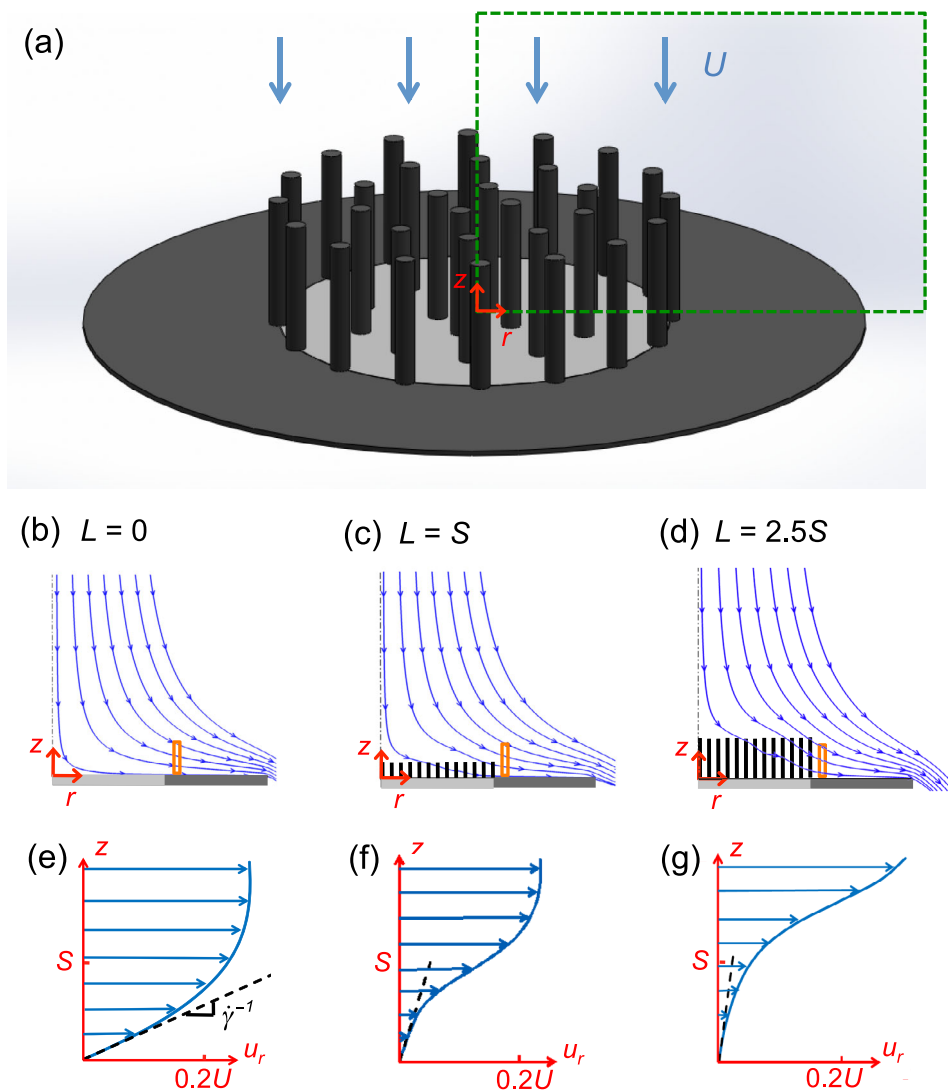
Fig. 5. Hairs greatly reduce airflow at eye surface. (a) Schematic of the computational model used in simulation. Dashed box shows cross section of flow from which streamlines are shown. (b–d) Numerical predictions for streamlines for (b) $L = 0$, (c) $L = S$, and (d) $L = 2.5S$. Solid box shows the location of the velocity profiles in (e–g). (e–g) Numerical predictions for velocity profiles for (e) $L = 0$, (f) $L = S$, and (g) $L = 2.5S$.

Computational simulation allows us to take a close look at the streamlines and velocity profiles at the eye surface for different hair lengths. The computational model is shown schematically in Fig. 5a. The streamlines associated with our numerical results are given in Fig. 5b–d. Only half the flow is shown because streamlines are axisymmetric around the center of the eye. In Fig. 5e–g we show how the radial velocity u_r varies with height z above the eye surface. The streamlines and velocity profiles are shown for 3 different hair lengths, $L/S = 0$, 1, 2.5.

Figure 5b,e show the streamlines and flow profile for an eye with no hair. The results are consistent with theoretical solutions for a viscous flow near a stagnation

point, where successive streamlines veer horizontally as they approach the eye [81]. Cross-sections of flow have a nearly parabolic velocity profile. The slope of the dashed line indicates the inverse of the shear rate $\dot{\gamma}$ at the ocular surface, and dictates the shear force exerted onto the eye surface.

When hairs are added to the eye surface, both the streamlines and velocity profile are changed drastically. For hair length $L/S = 1$, we observe the bulk of the flow veering horizontally before it gets close to the eye surface, as shown by Fig. 5c,f. As shown in the velocity profile, there is much less air traveling immediately above the eye surface. This decrease in airflow results in a decrease in shear rate $\dot{\gamma}$. As the hairs become longer the flow is turned away farther away from the eye surface, as shown by Fig. 5d,g. However, this only results in a slight reduction in shear rate since the presence of hairs, regardless of length, creates a stagnant zone of air between the hairs and immediately above the eye surface. The transition to the freestream bulk flow is shifted away from the eye with increased hair length, but this does not greatly affect the profile at the eye surface, as evidenced by comparing Fig. 5f,g.

3.4 Synthetic micro-pillars divert airflow

The diversion of airflow observed for the ocular hairs of insects may inform designs that help keep man-made equipment free from airborne particle deposition. Synthetic structures mimicking insect ocular hairs could be implemented on the sensitive surfaces of equipment like sensors. In turn, we determine if synthetic, hair-like structures can also divert airflow to protect surfaces.

Following the fabrication procedure outlined in Sect. 2.5, we create multiple micro-pillar arrays with piezo-resistive cantilever airflow sensors. By placing them in a small wind tunnel, we test the effects of pillar length L, pillar spacing S, and wind direction α on the pressure difference ΔP imposed by the incoming flow, as defined in Fig. 4c. In Fig. 4d, we see that the differential pressure ΔP decreases as pillars increase in length L/S. The trend is similar to that measured in previous experiments and simulations in Fig. 4b. However, with these experiments we can measure the effect of hairs on nearly horizontal ($\alpha = 5$ deg) flows. Using these microfabrication techniques, we can also test lengths below $L/S = 1$, which is the lower limit of our insect eye mimics in Fig. 2a. From our results, we see that even at a flow direction of $\alpha = 5°$ the hairs prevent airflow from reaching the surface. A reduction in differential pressure of 50% is observed for lengths of $L/S \geq 0.5$.

4 Discussion

In this study, we investigated a passive mechanism to maintain the cleanliness of compound eyes. Wind tunnel experiments and numerical simulation were used to determine the effects of insect eye hairs on the incoming airflow. In both experiments and simulation, the presence of hairs drastically decreased airflow at the eye surface, evidenced by a decrease in evaporation rate and shear rate, respectively. While the insect eye is not wet, measuring evaporation rate provides a metric for the shear rate imposed by the surrounding airflow. When air flows over water, the shear forces at the interface cause the water to evaporate. The evaporation rate is directly related to the shear rate [80]. Decreases in shear rate are attributed to decreases in particle deposition velocity [79]; therefore, the presence of hairs help to reduce particle deposition onto the surface of the compound eye.

From our wind tunnel experiments, represented by the blue and red crosses in Fig. 4b, we see that the presence of hairs decreases the evaporation rate by up to 90%.

A previous study found that decreased rates of evaporation using a similar experimental technique coincided with decreased rates in particle deposition [22]. Similarly, numerical simulations, represented by the black open points in Fig. 4b, show that there is a drastic decrease in airflow with the presence of hair, especially for the lower Reynolds number flow experienced by the fruit fly. The array of hairs provide a resistance to the incoming airflow and divert it away from the surface of the eye. This effect is similar to what has been found to occur for the antennae of the luna and silkworm moths [19,20] and the bristled wings of thrips [21].

Previous work by Brinkman [82] and Larson & Higdon [83] find that the velocity of a fluid as it enters an infinite array of cylinders parallel to the flow decreases exponentially with penetration depth. The decay of evaporation and shear rate observed for the low Reynolds number $Re = 9$ in Fig. 4b approximately follows an exponential decay. The exponential curve of best-fit for the experimental data, represented by the solid blue line in Fig. 4b, has a coefficient of determination $R^2 = 0.97$. The theory derived by Brinkman is for a viscous flow with a low Reynolds number, or Stokes flow, so it agrees well with our data for $Re = 9$. Therefore, the arrayed hairs, just like cylinders, reduce the amount of flow reaching the eye surface.

From our evaporation experiments and numerical simulation in Fig. 4b, we find that hair-like structures protect the ocular surface from airflows perpendicular to the ocular surface, while results from experiments with our synthetic micro-pillars in Fig. 4d show that they can also protect from near parallel flows. Since the surface of an insect's eye is curved, different sections of the eye will experience flows perpendicular and parallel to the surface. Thus, ocular hairs protect the insect's eye from flows both perpendicular and parallel to the eye surface.

From anatomical measurements in Fig. 1d, hair length appears to be consistent with spacing, even as the length varies across an order of magnitude. Our previous study found that eyelashes of an optimal length reduce tear film evaporation and deposition [22]. Unlike the circumferential array of hair found in eyelashes, the interspersed array on the compound eye of insects does not have an optimal length. Beyond $L = S$, the evaporation and shear rate remain constant. Therefore, the insect species with $L > S$ do not experience greater reductions in airflow at the eye surface. A possible advantage to longer hair is the increase in potential storage energy for catapulting deposited particles off [24]. The honey bee, an insect species that on average encounters up to five times its body mass in pollen per day [78], has $L = 3.4S$. These long ocular hairs more closely resemble the lengths found throughout the rest of the body.

We have found that protection against airborne particles may be one potential function for ocular hairs. In addition, these hairs could be multi-functional. Several previous workers found these hairs to be mechanosensory [4,7–9]. In honey bees they may be involved in sensing airflow and aiding in flight control [7,8]. While in crickets they serve as triggers for eye and head grooming [9]. Upon close inspection of the insect species possessing ocular hairs in Table 1, we notice that 13 of the 18 species are confirmed pollinators or flower visitors. Pollen collected directly from plants has a thin, viscous layer of fluid called pollenkitt [84]. This sticky fluid attracts pollinating insects to the pollen grains through odor and provides capillary adhesion so the grains remain attached to the insect. The ocular hairs may provide extra surface area for the pollenkitt to adhere to, as well as suspend pollen away from the surface for easier removal.

In our experiments and simulations we use stiff members to represent the insect ocular hairs. We find the ocular hairs are effectively rigid when exposed to flow associated with the Reynolds number of the fruit fly and forage looper moth during flight. The ratio of viscous to elastic forces [85] is $\frac{256\mu L^3 U}{Eh^4 \ln\left(\frac{2L}{h}\right)} \sim 10^{-3}\text{–}10^{-2}$, where

μ is the dynamic viscosity of air and $E = 3.05\,\mathrm{GPa}$ is the modulus of elasticity of insect cuticle [86]; the ratio of inertial and elastic forces [87] is $\frac{\rho U^2 L^3}{Eh^3} \sim 10^{-5}\text{–}10^{-4}$, indicating typical air flow has a negligible effect on hair deflection. Here, we assume the hair is rigidly attached at the base. However, sensory hairs have flexible bases that allow them to pivot and deform the anchoring tissue. Special cells located at the base behave like strain sensors and can quantify the hairs deflection based on the tissues deformation. These hairs are therefore capable of measuring forces. The flexibility of the base can be tuned to measure airflow, as has been found for crickets and spiders [88].

We successfully fabricated pillar arrays of the same scale as those found on the compound eyes of insects. However, we found that there were some limitations to our wind tunnel experiments. In particular, for nearly perpendicular airflows ($\alpha = 90$ deg), the sensor would always read the same differential pressure ΔP. However, for nearly horizontal flows ($\alpha = 5$ deg), the sensor reads differences in the differential pressure ΔP, as expected. We believe that for normally impinging flows, the sensors read the dynamic pressure of the freestream flow, rather than the local flows on the surface and in between the pillars because dynamic pressure dominates over form drag for blunt objects. On the other hand, for near shearing flows, the sensors bend in response to the pressure from the local airflow. We also found that both of the airflow sensors read the same pressure difference ΔP, even though one is in between the pillars and the other is directly underneath one of the pillars. Therefore, the differential pressure ΔP across the surface dominates over the pressure exerted onto the pillars.

Future studies should be pursued to directly measure the number of airborne particle impacting a surface with hair arrays. The experiments could follow those previously conducted by the authors [89]. In these experiments, a microcantilever was used to measure the number of particles impacting the sensor when exposed to a particle-laden flow. Hair arrays could be fabricated onto the surface of the microcantilever to see if there is a reduction in the number of particle impacts.

With future technologies, this study on micro-cleaning mechanisms can lead to bio-inspired designs aimed at maintaining micro-electronic devices clean. Devices such as Micro Aerial Vehicles (MAVs), microelectromechanical systems (MEMS), camera sensors and lenses, and solar panels may encounter harmful micro-scale particles during their use, and would benefit from efficient passive cleaning mechanisms to reduce malfunctions.

5 Conclusion

In this study, we investigated the function of the ocular hairs of insects. We performed a combination of wind tunnel experiments, numerical simulation and microfabrication of at-scale insect ocular hairs. We observed a minority of insects possess ocular hairs, but among those that do, hair length is equal to hair spacing. Wind tunnel experiments and computational fluid simulations find that this hair length provides reduction of airflow of 90% when air impinges the eye surface normally. Greater hair lengths provide diminishing returns for reduction of airflow. Experiments with our micro-fabricated ocular hairs show that 50% reduction of airflow occurs for shear flow, air traveling parallel to the eye surface. A reduction of flow is accompanied by reduction of particle deposition. Structures inspired by the ocular hairs may be useful in protecting the sensitive surfaces of sensors in order to help extend their usable life.

References

1. M.V. Srinivasan, S. Zhang, Ann. Rev. Neurosci. **27**, 679 (2004)
2. L.F. Tammero, M.H. Dickinson, J. Exper. Biol. **205**, 2785 (2002)
3. A. Sourakov, Florida Entomologist **94**, 367 (2011)
4. H. Hinton, Roy Entomol. Soc. London Symp. (1970)
5. M.F. Land, R.D. Fernald, Ann. Rev. Neurosci. **15**, 1 (1992)
6. W.H. Miller, G.D. Bernard, J.L. Allen, Science **162**, 760 (1968)
7. V. Neese, Z. Vergleichende Physiol. **49**, 543 (1965)
8. V. Neese, Z. Vergleichende Physiol. **52**, 149 (1966)
9. H.-W. Honegger, Cell Tissue Res. **182**, 281 (1977)
10. M.M. Perry, J. Morphol. **124**, 249 (1968)
11. F.G. Barth, Curr. Opin. Neurobiol. **14**, 415 (2004)
12. J. Casas, T. Steinmann, G. Krijnen, J. Royal Soc. Interface **7**, 1487 (2010)
13. R. Fettiplace, C.M. Hackney, Nat. Rev. Neurosci. **7**, 19 (2006)
14. A. Bejan, J. Heat Transfer (Transactions ASME, Ser. C) **112**, 662 (1990)
15. A. Battisti, G. Holm, B. Fagrell, S. Larsson, Ann. Rev. Entomol. **56**, 203 (2011)
16. M.S. Mooring, W.M. Samuel, Behaviour **135**, 693 (1998)
17. D.I. Rubenstein, M. Koehl, Am. Naturalist 981 (1977)
18. M. Lippmann, D. Yeates, R. Albert, Br. J. Ind. Med. **37**, 337 (1980)
19. S. Vogel, J. Insect Physiol. **29**, 597 (1983)
20. C. Loudon, E.C. Davis, J. Chem. Ecol. **31**, 1 (2005)
21. K. Sato, H. Takahashi, M.-D. Nguyen, K. Matsumoto, I. Shimoyama, 2013 IEEE 26th International Conference on Micro Electro Mechanical Systems (MEMS), 21 (2013)
22. G.J. Amador, et al., J. Royal Soc. Interface **12**, 20141294 (2015)
23. J.B. Benoit, Aestivation (publisher Springer, 2010), p. 209
24. G.J. Amador, D.L. Hu, J. Exper. Biol. **218**(20), 3164 (2015)
25. M. Streinzer, A. Brockmann, N. Nagaraja, J. Spaethe, PloS One **8**, 57702 (2013)
26. Diptera.info. Chrysotoxum elegans. `http://www.diptera.info/forum/attachments/img-0837_1.jpg`
27. A. Karawath, User:Aka/Images/Animals. `https://commons.wikimedia.org/wiki/User:Aka/Images/Animals`
28. D. Coetzee, `https://commons.wikimedia.org/wiki/File:Lucilia_sericata_on_doorknob_-_detail_of_fly.jpg`
29. L. Howard, `http://remf.dartmouth.edu/images/insectPart3SEM/`
30. Alamy, `http://www.alamy.com/stock-photo-gnat-culex-pipiens-the-common-house-mosquito-top-dorsal-view-51307101.html`
31. A. Cockburn, `http://www.tirpor.com/cpg_public/`
32. P. Waters, `http://www.shutterstock.com/pic-77748943/stock-photo-western-honey-bee-in-flight-with-sharp-focus-on-its-head-isolated-on-white.html?src=tQhZhOTnaTzj6X4vDyIFrA-1-24`
33. Karlsson, C. Musca domestica @ 5X. `https://www.flickr.com/photos/conkar/6792723054/`
34. Diptera.info. Chrysotoxum intermedium. `http://www.diptera.info/forum/attachments/ev-chrysotoxum-intermedium.jpg`
35. wiseGEEK. `http://www.wisegeekhealth.com` what-is-an-occipital-lymph-node.htm#very-close-view-of-mosquito-on-human-skin
36. A.R. Parker, Z. Hegedus, R.A. Watts, Proc. Royal Soc. London. Series B: Biol. Sci. **265**, 811 (1998)
37. S.D. Carlson, C. Chi, Cell Tissue Res. **149**, 21 (1974)

38. D.G. Stavenga, S. Foletti, G. Palasantzas, K. Arikawa, Proc. Royal Soc. B: Biological Sci. **273**, 661 (2006)
39. A. Oliva, A new species Oxelytrum Gistel (Coleoptera, Silphidae) from southern Argentina, with a key to the species genus. ZooKeys 1 (2012)
40. S. Fischer, C.H. Mueller, V.B. Meyer-Rochow, Visual Neurosci. **28**, 295 (2011)
41. M.W. Szyndler, K.F. Haynes, M.F. Potter, R.M. Corn, C. Loudon, J. Royal Soc. Interface **10**, 20130174 (2013)
42. T. Bourguignon, Y. Roisin, ZooKeys, 55 (2011)
43. S. Zonstein, Y.M. Marusik, (Araneae, Palpimanidae) ZooKeys, 27 (2013)
44. G.S. Paulson, `http://webspace.ship.edu/gspaul`
45. M. Smith, Part III – Human Eyes and Insect Eyes: A 3D modelling article. `http://www.microscopy-uk.org.uk/mag/artjun10/mol%-eyes1.html`
46. A. Osterrieder, `http://www.plantcellbiology.com` 2012 02
47. California Department Food Agriculture Novakia miloi kerr `http://www.cdfa.ca.gov/plant/ppd/Lucid/Novakia/key/Novakia/Media/Html/N_miloi.htm`
48. The University Virginia Virtual Lab. `http://www.virlab.virginia.edu/nanoscience_class Nanoscience_class.htm Lab`
49. D. Gregory, D. Marshall, `http://wellcomeimages.org/indexplus/image/B0000664.html`
50. The University Texas at Dallas Department Geosciences. `https://www.utdallas.edu/ pujana/sem/ant1.htm.`
51. Euchoo. Boliaology Part 01. `http://euchoo.net/blog.bk/Boliaology-Part01`
52. Biology Department at Swarthmore College. The Robert Savage Image Award At Swarthmore College. `https://savageimageaward.wordpress.com/`
53. Gans, M. `http://murry-gans.blogspot.com/2012_12_01_archive.html`
54. Howard, L. Insect Part 1 SEM. `http://remf.dartmouth.edu/images/insectPart1SEM/`
55. Midwood Sci. SEM. `http://midwoodscience.org/sem/2012/`
56. S. Vogel, J. Exper. Biol. **44**, 567 (1966)
57. H. Davies, C.A. Butler (Rutgers University Press, 2008)
58. S. Succi (Oxford University Press, 2001)
59. C.K. Aidun, J.R. Clausen, Ann. Rev. Fluid Mech. **42**, 439 (2010)
60. A.J.C. Ladd, R. Verberg, J. Statist. Phys. **104**, 1191 (2001)
61. Z.G. Mills, W. Mao, A. Alexeev, Trends BioTechnol. **31**, 246 (2013)
62. E. Gauger, H. Stark, Physical Rev. E **74** (2006)
63. H. Jian, A.V. Vologodskii, T. Schlick, J. Comp. Phys. **136**, 168 (1997)
64. C.S. Peskin, Acta Numerica **11**, 479 (2002)
65. M. Bouzidi, M. Firdaouss, P. Lallemand, Phys. Fluids **13**, 3452 (2001)
66. R. Ghosh, G.A. Buxton, O.B. Usta, A.C. Balazs, A. Alexeev, Langmuir **26**, 2963 (2009)
67. J. Branscomb, A. Alexeev, Soft Matter **6**, 4066 (2010)
68. C. Semmler, A. Alexeev, Phys. Rev. E **84**, 066303 (2011)
69. Z.G. Mills, B. Aziz, A. Alexeev, Soft Matter **8**, 11508 (2012)
70. H. Takahashi, N.M. Dung, K. Matsumoto, I. Shimoyama, J. Micromech. Microeng. **22**, 055015 (2012)
71. H. Takahashi, K. Matsumoto, I. Shimoyama, Measur. Sci. Technol. **24**, 055304 (2013)
72. M. Gel, I. Shimoyama, J. Micromech. Microeng. **14**, 423 (2004)
73. N. Thanh-Vinh, H. Takahashi, K. Matsumoto, I. Shimoyama, Sensors Actuators A: Physical (2014)
74. C. Chi, S.D. Carlson, Cell Tissue Res. **166**, 353 (1976)
75. L. Sedda, et al., Proc. Royal Soc. B: Biological Sci. **279**, 2354 (2012)
76. J.H. Fewell, Behavioral Ecol. Sociobiol. **22**, 401 (1988)
77. M.W. Davidson, `http://micro.magnet.fsu.edu/optics/olympusmicd/galleries/darkfield/muscadomestica1.html`
78. M.L. Winston, *The Biology of the honey bee* (Harvard University Press, 1991)
79. T. Schneider, M. Bohgard, Indoor Air **15**, 215 (2005)

80. T.L. Bergman, F.P. Incropera, A.S. Lavine, D.P. DeWitt, *Fundamentals Heat and Mass Transfer* (John Wiley, Sons, 2011)
81. H. Schlichting, K. Gersten, *Boundary-layer theory* (Springer, 2000)
82. H. Brinkman, Appl. Scientific Res. **1**, 27 (1949)
83. R. Larson, J. Higdon, J. Fluid Mech. **166**, 449 (1986)
84. E. Pacini, M. Hesse, Flora-Morphology, Distribution, Funct. Ecol. Plants **200**, 399 (2005)
85. L. Guglielmini, A. Kushwaha, E.S. Shaqfeh, H.A. Stone, Phys. Fluids **24**, 123601 (2012)
86. J.-H.Dirks, D. Taylor, J. Exper. Biol. **215**, 1502 (2012)
87. E. De Langre, Ann. Rev. Fluid Mech. **40**, 141 (2008)
88. J.A. Humphrey, F.G. Barth, Adv. Insect Physiol. **34**, 1 (2007)
89. H. Takahashi, T. Kan, K. Matsumoto, I. Shimoyama, IEEE Inter. Conf. Micro Electro Mech. Sys. (MEMS) (in preparation)